



Reduction Mechanism of Solid Electrolyte Interphase Formation on Lithium Metal Anode: Fluorine-Rich Electrolyte

Yu Wu, Qintao Sun, Yue Liu, Peiping Yu, Bingyun Ma, Hao Yang, Miao Xie, and
Tao Cheng^{a,z} 

Institute of Functional Nano and Soft Materials (FUNSOM), Soochow University, Suzhou 215123, People's Republic of China

Metallic lithium is considered a promising anode that can significantly increase the energy density of rechargeable lithium-based batteries, but problems like uncontrollable growth of lithium dendrites and formation of dead lithium impede its application. Recently, a low-concentration single-salt two-solvent electrolyte, 1 M LiTFSI/FDMA/FEC, has attracted attention because a high coulombic efficiency can be achieved even after many cycles owing to the formation of a robust solid electrolyte interface (SEI). However, the reaction mechanism and SEI structure remain unclear, posing significant challenges for further improvement. Here, a hybrid *ab initio* and reactive force field (HAIR) method revealed the underlying reaction mechanisms and detailed formation pathway. 1 ns HAIR simulation provides critical information on the initial reduction mechanism of solvent (FDMA and FEC) and salt (LiTFSI). FDMA and FEC quickly decompose to provide F⁻ that builds LiF as the major component of the inner layer of inorganic SEI, which has been demonstrated to protect Li anode. Decomposition of FDMA also leads to a significant nitrogen-containing composition, producing Li-N-C, Li_xN, and other organic components that increase the conductivity of SEI to increase performance. XPS analysis confirms evolution of SEI morphology consistent with available experiments. These results provide atomic insight into SEI formation, which should be beneficial for the rational design of advanced electrolytes.

© 2022 The Electrochemical Society ("ECS"). Published on behalf of ECS by IOP Publishing Limited. [DOI: [10.1149/1945-7111/ac44bc](https://doi.org/10.1149/1945-7111/ac44bc)]

Manuscript submitted October 20, 2021; revised manuscript received December 15, 2021. Published January 5, 2022. *This paper is part of the JES Focus Issue on Energy Storage Research in China.*

Supplementary material for this article is available [online](#)

In the last three decades, lithium (Li)-ion batteries (LIBs) have risen to prominence as one of the most effective electrochemical energy storage technologies, drastically altering our daily life.^{1–4} LIBs' success is aided by their long cycle life, high energy efficiency, high energy density, little self-discharge, and other merits.⁵ As the manufacturing process improves, the energy density of LIBs approaches its theoretical limit. As a result, there is a renewed interest in rechargeable Li metal batteries in the scientific and industrial worlds (LMBs).

With the lowest electrochemical potential of -3.04 V (vs standard hydrogen electrode) and ultrahigh theoretical specific capacity of 3860 mAh.g⁻¹ of metallic Lithium, lithium metal batteries (LMBs) with metallic Lithium as anodes are the most promising candidate to replace LIBs.^{6–10} However, the realization of lithium metal anodes faces great challenges. Owing to uncontrollable extreme side reactions between lithium metal and electrolyte, highly porous and dendritic lithium deposition morphology not only results in low lithium utilization rate and poor cycle life, but also poses a severe safety hazard.^{11–13}

Because the chemical composition of electrolytes might impact Li dendrite formation, it's important to create electrolytes that are stable with Li or react with Li to generate a homogeneous, robust solid electrolyte interface (SEI).⁷ Detailed solvation structure has significant influence to the reactivity. For example, Chen et al. reported a thorough investigation of Ion-solvent complexes in reducing the reductive stability of electrolyte.¹⁴ The influence to SEI reaction can be either simulated in an *ab initio* manor, or the emerging data driven approach.¹⁵ More atomic insights into the fundamental interactions in lithium battery electrolytes has been well summarized by Chen et al.¹⁶ A robust SEI can serve as a protective layer that blocks further side reactions between Lithium metal anode (LMA) and electrolytes.^{17,18} Increasing the safety and Coulombic efficiencies (CEs) in LMBs by adjusting the components of SEI to stable, dense, and homogenous layers on LMA is a potential

approach to facilitate LMBs. There have been numerous researches on the impact of electrolytes on SEI.^{19–23}

Recently, amide compounds, which typically have a -NR₂ amide group, have been added to LMBs as a new electrolyte additive, with the expectation of forming fewer low ion-conductive inorganic constituents than traditional -OR₂ ester groups solvents like ethylene carbonate (EC) and dimethyl carbonate (DMC).^{24,25} Wang. et al.²⁴ compared an amide solvent (2,2,2-Trifluoro-N, N-dimethylacetamide, FDMA) with traditional electrolyte system (EC and DMC) in LMBs, and demonstrates that the battery with FDMA additive exhibit significantly increased cycling stability and high CEs. In their work, they also carried out X-ray photoelectron spectroscopy (XPS) with combination of quantum mechanics (QM) calculations to analysis the SEI components. Although some qualitative findings have been obtained, providing atomic details on the underlying chemical process using existing experimental characterization methods remains exceedingly difficult, which greatly impedes the development of improved electrolytes. Techniques that can offer this level of detail are in high demand right now.

It has been demonstrated the quantum mechanics (QM) based molecular dynamics (MD) simulation can simulate the reaction process in SEI formation by providing insight at the atomic level.^{26–28} SEI simulation is a typical multiscale problem that requires multiscale simulation. Shi et al. have well documented the multiscale simulation methods and their applications in lithium-ion battery research.²⁹ development *Ab initio* molecular dynamics (AIMD) simulation with forces from density functional theory (DFT) can accurately simulate reaction process.³⁰ However, the time scale of AIMD simulation usually limited within dozens of picoseconds (ps) due to its high computational cost, but still far from meeting the requirement of simulating SEI formation that requires long time-scale simulation with the accuracy at QM level.^{31,32} Reactive force field (ReaxFF) has been designed to describe the formation and discontinuity of chemical bonds. ReaxFF based on bond order which was proposed by van Duin et al. is an effective way to simulate the reaction process especially in large time scales reaction simulation.^{33,34} Therefore, ReaxFF bridges the gap between QM and non-reactive empirical force field based molecular simulation methods.

Hybrid *ab initio* and reactive force field molecule dynamics (HAIR) are proposed by Liu. et al. which takes advantage of AIMD

^aInstitute of Functional Nano & Soft Materials (FUNSOM), Jiangsu Key Laboratory for Carbon-Based Functional Materials & Devices, Soochow University, 199 Ren'ai Road, Suzhou, 215123, Jiangsu, People's Republic of China.

^zE-mail: tcheng@suda.edu.cn

and ReaxFF MD simulation, and has been applied in LMBs systems to study the reaction of electrolytes and lithium anodes during charge and discharge process.^{35,36} In HAIR method, AIMD is employed to describe the local electrochemical reaction accurately, what's more, the role of ReaxFF MD could accelerate the chemical reactions and mass transfer, which ensures HAIR method can simulate the SEI formation on a relatively large time scale with an affordable cost while keeping a high accuracy.

In this work, we choose an F-rich electrolyte with amide solvents in lithium metal battery, which is Lithium bis(trifluoromethanesulfonyl)imide in a mixture of 2,2,2-Trifluoro-N, N-dimethylacetamide and fluoroethylene carbonate (LiTFSI/FDMA/FEC). We employ HAIR method proposed by Liu et al. to study reaction process and the role of amide solvents in this SEI formation. In addition, 1 ns SEI simulation and XPS was performed.

Simulation Methods

The AIMD simulation used the Perdew–Burke–Ernzerhof (PBE) functional to describe the electron exchange and correlation energies within the generalized gradient approximation (GGA).³⁷ To describe

the London dispersion integrations, we added the Grimme D3 correction.³⁸ The projector augmented wave (PAW) method as implemented in VASP was utilized.³⁹ A $1 \times 1 \times 1$ Monkhorst–Pack k-point mesh was used to sample the Brillouin zone integration, and we chose a 400 eV energy cutoff for plane-wave basis expansion.⁴⁰ We used a Gaussian smearing width of 0.2 eV. The threshold for the electronic structure convergence of the self-consistent field was set to 10^{-4} eV.

ReaxFF molecular dynamics (RMD) simulations are carried out by using the Large-scale Atomic/Molecular Massively Parallel Simulator (LAMMPS 2018)⁴¹ package. It is used to conduct 5 ps long simulation for one cycle in HAIR method. To guarantee good energy conservation while ensuring efficient converge for collisions and smooth reactions, we choose a proper 0.25 fs timestep in this work. And NVT ensemble at 300 K, which fixes the molecule numbers (N), volume (V), and temperature (T) are employed during HAIR simulations.

Before the HAIR simulation, we usually test the AIMD simulation and ReaxFF MD for a short period of time to determine the reasonableness and applicability of the model and field parameters we choose. In the HAIR procedure, the time steps for AIMD and

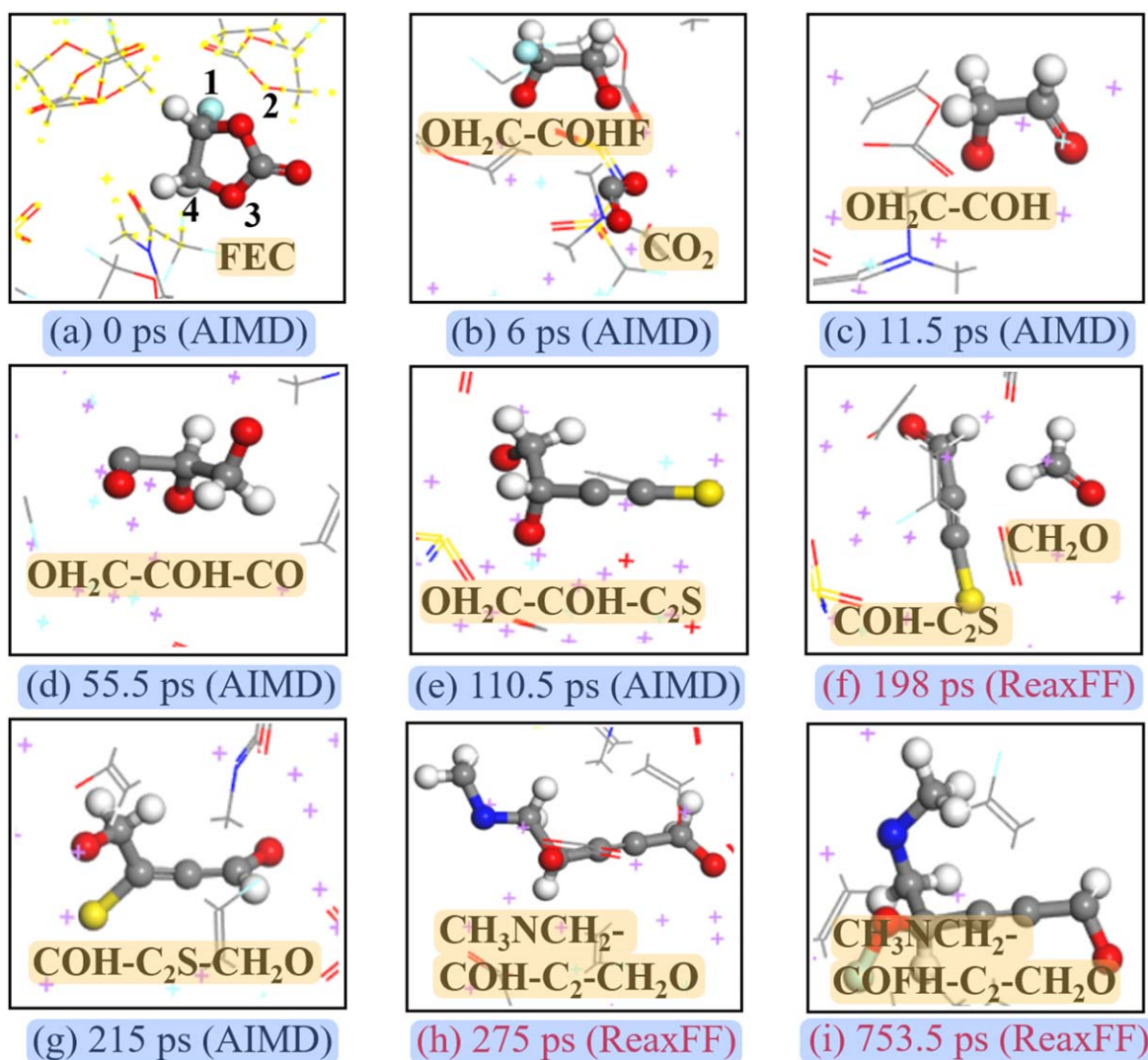


Figure 1. Sequence of FEC (Pathway1) decompositions obtained from Hybrid simulations between 0 and 753.5 ps (FEC to $\text{CH}_3\text{NCH}_2\text{-COFH-C}_2\text{CH}_2\text{O}$). (a) 0 ps, (b) 6 ps, (c) 11.5 ps, (d) 55.5 ps, (e) 110.5 ps, (f) 198 ps, (g) 215 ps, (h) 275 ps and (i) 753.5 ps. The red 198 ps, 275 ps and 753.5 ps were observed in ReaxFF MD. The black 6 ps, 11.5 ps, 55.5 ps, 110.5 ps and 215 ps were observed in AIMD simulation. Color code: lithium, purple; oxygen, red; carbon, gray; fluorine, cyan; sulfur, yellow; nitrogen, blue; hydrogen, white.

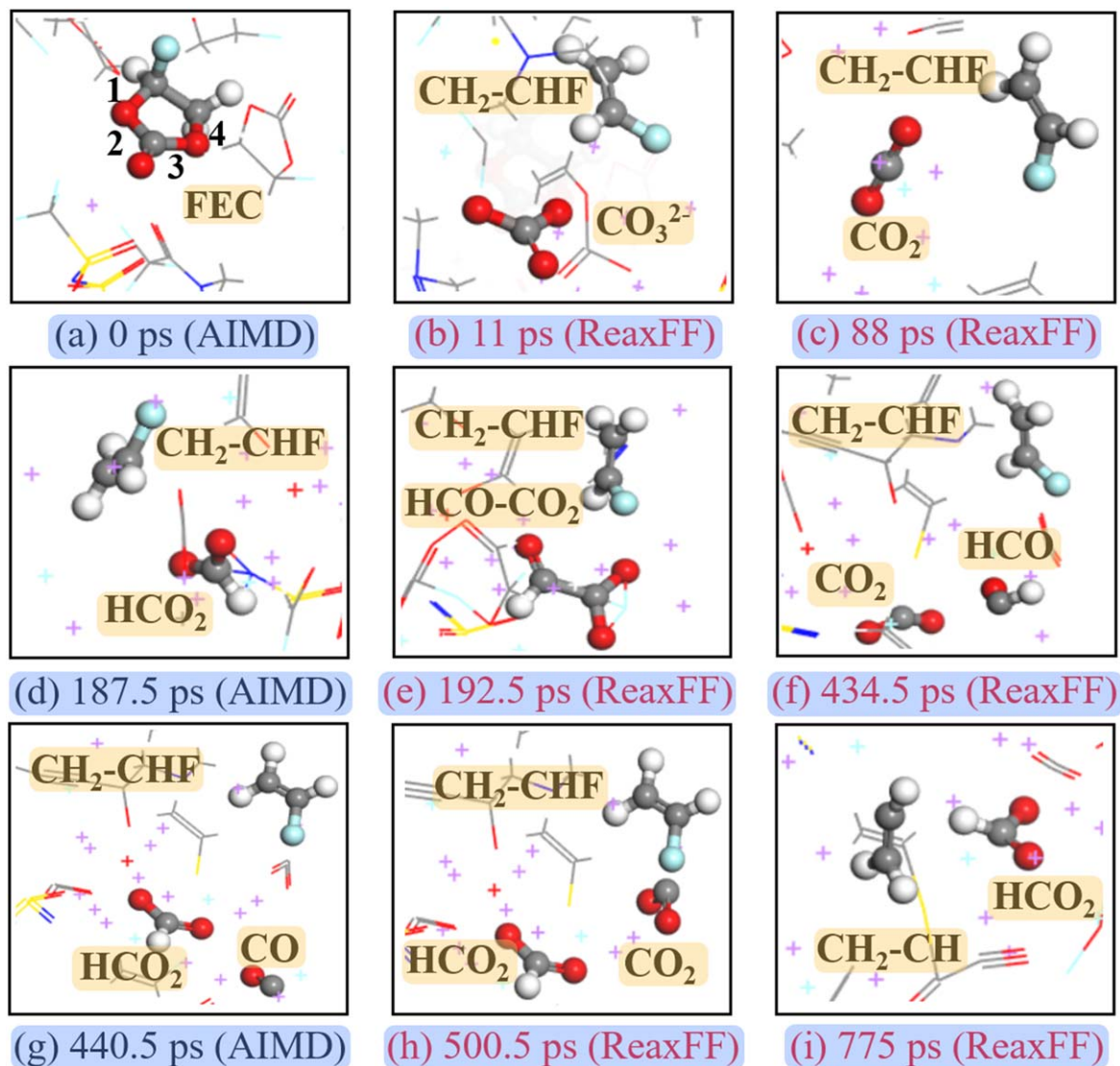


Figure 2. Initial reductive reaction pathways of FEC (Pathway 2) obtained from HAIR simulations between 0 and 775 ps (FEC to $\text{CH}_2\text{-CH}$, HCO_2 and CO_2). (a) 0 ps, (b) 11 ps, (c) 88 ps, (d) 187.5 ps, (e) 192.5 ps, (f) 434.5 ps, (g) 440.5 ps, (h) 500.5 ps and (i) 775 ps. The red 11 ps, 88 ps, 192.5 ps, 434.5 ps, 500.5 ps and 775 ps were observed in ReaxFF MD. The black 187.5 ps, and 440.5 ps were observed in AIMD simulation. Color code: lithium, purple; oxygen, red; carbon, gray; fluorine, cyan; sulfur, yellow; nitrogen, blue; hydrogen, white.

ReaxFF were set at 0.1 and 0.25 fs, respectively, to guarantee good energy conservation during the HAIR simulations while ensuring efficient convergence for collisions and smooth reactions. The HAIR simulations were conducted for 140 cycles (770 ps) with 10-time acceleration in initial short time test. Due to the slow reaction in the later stage of simulation, the product hardly changes. To reduce computational costs, we use 100 times acceleration to scale up the simulation to more than 1 ns.

Model of the lithium-electrolyte system.—The Li-metal anode was represented by a 6-layer (3×3) supercell slab, where two of the bottom layers of the slab were fixed (Fig. S1 (available online at stacks.iop.org/JES/169/010503/mmedia)) with the most stable Li (100) surface. To achieve the desired concentrations of Li-salts in the electrolyte, we used 1 molecule LiTFSI dissolved in 4 FDMA and 6 FEC solvents to represent 1 M LiTFSI/FDMA/FEC electrolyte systems. The final simulation periodic cell was $10.5 \times 10.5 \times 26.5$ Å, approximately.

XPS simulation details.—The calculated method of binding energy is under the initial state approximation that has been implemented in VASP at PBE-D3 level.^{38,42,43} To simulate the intensity of XPS figures, a thousand AIMD trajectories were used to calculate the binding energy. In this simulation, to gather Figs. 7a, 7b, a thousand AIMD trajectories at the vicinity of 550 ps were used, and to gather Figs. 7c, 7d, a thousand AIMD trajectories at the vicinity of 1 ns were used. All of the calculated binding energies are classified by element, and the histogram of frequency distribution whose group distance is 0.1 eV is drawn according to the binding energy, and this statistical distribution histogram were used as the raw data to fit the XPS spectrum. Peak fitting is based on peak location and structure information in trajectories.

Results

FEC is better than EC, one of the most commonly used solvents, because FEC can also provide F whereas EC cannot. In 1 M LiTFSI/FDMA/FEC, we observed that the six FEC molecules exhibit

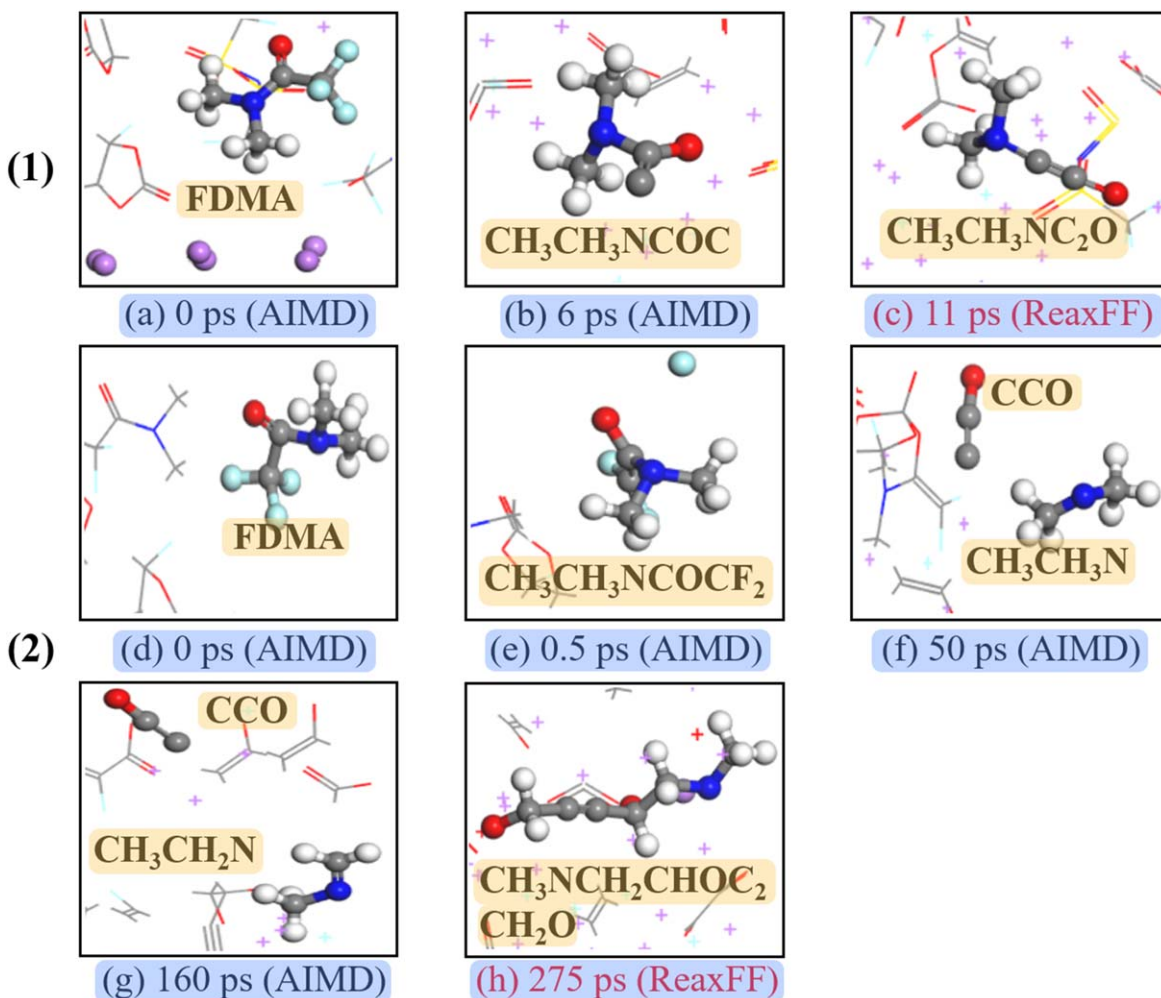


Figure 3. Initial reductive reaction pathways of FDMA obtained from HAIR simulations. (1) and (2) are possible decomposition pathways. (Pathway 1 : FDMA to $\text{CH}_3\text{CH}_3\text{NC}_2\text{O}$, Pathway 2: FDMA to $\text{CH}_3\text{NCH}_2\text{CHOC}_2\text{CH}_2\text{O}$). (a) and (d) 0 ps, (b) 6 ps, (c) 11 ps, (e) 0.5 ps, (f) 50 ps, (g) 160 ps and (h) 275 ps. The red 11 ps and 275 ps were observed in ReaxFF MD. The black 0.5 ps, 6 ps, 50 ps and 160 ps were observed in AIMD simulation. Color code: lithium, purple; oxygen, red; carbon, gray; fluorine, cyan; sulfur, yellow; nitrogen, blue; hydrogen, white.

different decomposition pathways due to different chemical environments, which can be distinguished into two main pathways. The first pathway is that FEC breaks the 2nd and 3rd C–O bonds at 6 ps to produce $\text{OH}_2\text{C}-\text{COHF}$ and CO fragments, and CO reacts with O separated from LiTFSI to form CO_2 (Fig. 1b). After 5.5 ps, the fragments of $\text{OH}_2\text{C}-\text{COHF}$ were removed from F to form $\text{OH}_2\text{C}-\text{COH}$ (Fig. 1c). At 55.5 ps, it reacts with the dissociated CO in LiTFSI to form $\text{OH}_2\text{C}-\text{COHCO}$ (Fig. 1d). $\text{OH}_2\text{C}-\text{COHCO}$ reacts with the separated CS in LiTFSI at 110.5 ps and then removes O to form $\text{OH}_2\text{C}-\text{COHC}_2\text{S}$ (Fig. 1e). The C–C bond was broken at 198 ps and broken into fragments $\text{COH}-\text{C}_2\text{S}$ and CH_2O (Fig. 1f). The broken fragments were reconstructed at 215 ps to form $\text{COH}-\text{C}_2\text{S}-\text{CH}_2\text{O}$ (Fig. 3g). The fragments are first stripped of S and then react with the FDMA product at 275 ps to form $\text{CH}_3\text{NCH}_2-\text{COH}-\text{C}_2\text{CH}_2\text{O}$ (Fig. 3h), and keeping the form of $\text{CH}_3\text{NCH}_2-\text{COFH}-\text{C}_2\text{CH}_2\text{O}$ until the end of the 1 ns simulation.

The second decomposition pathway is completely different from the first one. It first occurs (Fig. 2a) when the 1st and 4th C–O bonds are broken at 11 ps, forming CO_3^{2-} and CH_2-CHF fragments (Fig. 2b). Subsequent changes mainly occurred on CO_3^{2-} , after which one O was removed at 88 ps (Fig. 2c), and then reacted with the H released from FEC to form HCO_2 at 187.5 ps (Fig. 2d). Later,

it reacts with CO in FEC at 192.5 ps, breaking the C–O bond and then connecting the C–C bond to form $\text{HCO}-\text{CO}_2$ (Fig. 2e). The C–C bond breaks at 434.5 ps, resulting in HCO and CO_2 fragments (Fig. 2f). After 6 ps, CO_2 removes one O and HCO to form HCO_2 fragments, but CO separates from other FEC O to form CO_2 (Fig. 2h). At 775 ps, CH_2-CHF is removed from F to form CH_2-CH , and CO_2 remains unchanged until the simulation reaches 1 ns.

In order to improve the computational efficiency, HAIR method was turned on to simulate the reaction process of FDMA. The four FDMA molecules show three different decomposition pathways due to their different chemical environments. Figure 3 shows two decomposition pathways. For the first pathway, FDMA is located near the lithium metal layer (Fig. 3a). Firstly, all fluorine atoms are removed from FDMA at 6 ps (Fig. 3b), and consumed by Li atoms to form LiF, which is the main component of SEI. Then the O–C bond breaks at 11 ps, immediately, the Oxygen atom connects to another Carbon atom (Fig. 3c). After a long time simulation, the molecule remains unchanged. The second decomposition pathway showed significant differences. FDMA is located around the top and is surrounded by FEC and FDMA molecules (Fig. 3d). Similarly, the first step of the reaction is the removal of Fluorine atoms, and the

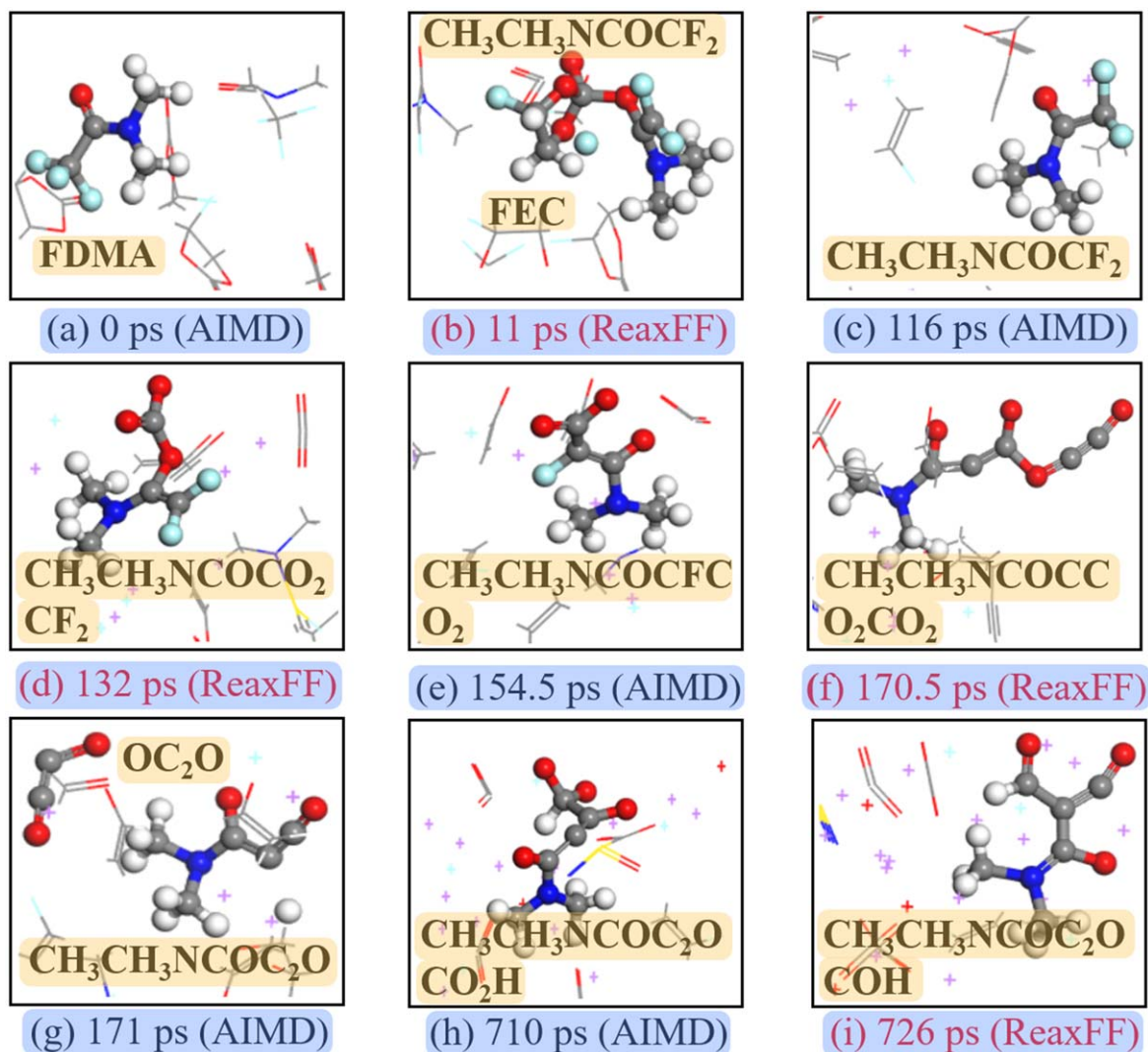


Figure 4. Initial reductive reaction pathways of FDMA obtained from HAIR simulations (Pathway 3: FDMA to $\text{CH}_3\text{CH}_3\text{NCOC}_2\text{OCHO}$). (a) 0 ps, (b) 11 ps, (c) 116 ps, (d) 132 ps, (e) 154.5 ps, (f) 170.5 ps, (g) 171 ps, (h) 710 ps and (i) 726 ps. The red 11 ps, 132 ps, 170.5 ps and 726 ps were observed in ReaxFF MD. The black 116 ps, 154.5 ps, 171 ps and 710 ps were observed in AIMD simulation. Color code: lithium, purple; oxygen, red; carbon, gray; fluorine, cyan; sulfur, yellow; nitrogen, blue; hydrogen, white.

first F is removed at 0.5 ps (Fig. 3e), and the N–C bond fracture occurred at 50 ps, resulting in fragments of CCO and CH_3NCH_3 (Fig. 3f). Fragment CH_3NCH_3 further removes one H at 160 ps (Fig. 3g), and then finally forms long chain $\text{CH}_3\text{NCH}_2\text{CHOC}_2\text{CH}_2\text{O}$ with the FEC fragments (Fig. 3h).

The third decomposition route is similar to the previous two in that it begins with the removal of F and ends with an entirely different breakdown. In these reactions, FEC and FDMA with one F removal occurs at 6 ps (Fig. 4b), and the two are broken and decomposed until 116 ps (Fig. 4c). Afterwards, the fragments of CO_2 produced by FEC react with $\text{CH}_3\text{CH}_3\text{NCOCF}_2$ at 132 ps to form $\text{CH}_3\text{CH}_3\text{NCOCO}_2\text{CF}_2$ (Fig. 4d), while the fragments are reconstructed at 154.5 ps, first disconnected from CO_2 , and then connected after removing an F (Fig. 4e). The subsequent reaction is to remove the last F and react with the fragment CCO produced by the previous FDMA at 170.5 ps to form $\text{CH}_3\text{CH}_3\text{NCOCCO}_2\text{CO}_2$ (Fig. 4f). Immediately after 0.5 ps, the C–O bond breaks to form OC_2O and $\text{CH}_3\text{CH}_3\text{NCOC}_2\text{O}$ fragments (Fig. 4g). The subsequent long-term simulations remain unchanged. Until 710 ps, the $\text{CH}_3\text{CH}_3\text{NCOC}_2\text{O}$ fragments react with the fragments HC_2O produced in the FEC to

form $\text{CH}_3\text{CH}_3\text{NCOC}_2\text{OCO}_2\text{H}$ (Fig. 4h). Finally, at 726 ps, one O is removed from the ends of the fragments to form $\text{CH}_3\text{CH}_3\text{NCOC}_2\text{OCHO}$ fragments (Fig. 4i).

Based on the initial reduction of electrolyte at the Li metal anode surface (Fig. 5a), the above simulations are further extended to be 1 ns (Fig. 5b), which consists of 770 ps HAIR simulation and 230 ps ReaxFF. Detailed analysis (Fig. 6) show that the HAIR prediction well agrees with the experimental results from Wang et al.²⁴ The decomposition products of the LiTFSI/FDMA/FEC electrolyte system are more ion-conducting nitrogen-containing components in addition to the common LiF and Li_2O . It has been hypothesized that LiF has a positive contribution in stabilizing SEI. Thus, increasing LiF has been applied as a design principle in SEI design. However, such assumption has been challenged by recent work, when the protected function of LiF was reported.⁴⁴ Our simulation shows that the robust inner inorganic layer (IIL) SEI formation requires a homogenous LiF layer, when high concentrated electrolyte can provide enough F^- to facilitate in situ construction. Thus, LiF formation itself does not necessitate a robust SEI, but the quantity and location of LiF are important. However, during the

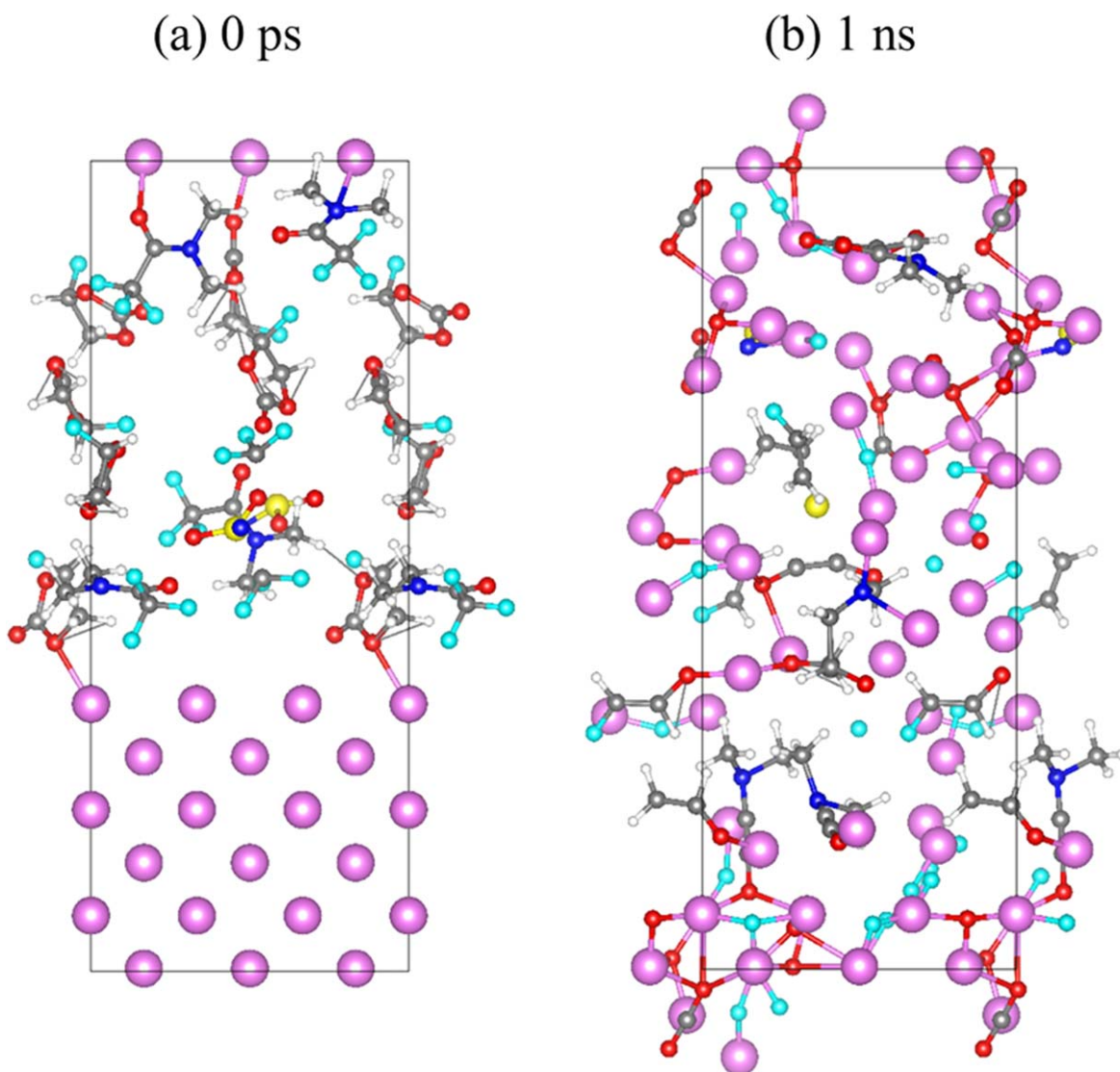


Figure 5. Snapshots from Hybrid simulation for 1 M LiTFSI/FDMA/FEC in (a) 0 ps and (b) 1 ns. Color code: lithium, purple; oxygen, red; carbon, gray; fluorine, cyan; sulfur, yellow; nitrogen, blue; hydrogen, white.

process of lithium plating/stripping, this kind of inorganic SEI with high mechanical strength is prone to cracks and lithium dendrites grow. Electrolytes based on amide containing nitrogen components will lead to denser lithium deposits and help reduce porous morphology, thereby inhibiting irreversible reactions, and helping to reduce the generation of lithium dendrites and dead Lithium.

The comparison of the simulated XPS with experiment, as shown in Fig. 7, demonstrates the prediction based on HAIR generated SEI structure are highly consistent with experiment, indicating that our simulated structure resembles the experimental structure quite well. Further analysis shows that the main inorganic component in SEI amorphous structure is LiF (Figs. 7b and 7d). The reduced N are in three forms: N-C₃, Li-N-C and Li_x-N, as shown in Figs. 7a and 7c. Among them, Li-N-C and Li_x-N have also been proved experimentally and N-C₃ mainly comes from the decomposition of FDMA. It's worth mentioning that although the simulation findings for 550 ps were found to be quite comparable to the experimental results, extending the simulation duration to 1 ns, on the other hand, can considerably enhance the consistency of the anticipated and

experimental findings (Fig. 7 and Table I). As a result, the above findings highlight the necessity of increasing the simulation time.

Conclusions

In summary, a hybrid scheme (HAIR) that combines ab initio and reactive molecular dynamics (RMD) is employed to explore the detailed reduction mechanism in the SEI formation process between a fluorine-rich electrolyte, 1 M LiTFSI/FDMA/FEC, and Li anode. The produced electrolyte combines FDMA and FEC as a co-solvent, demonstrating that the electrochemical performance of the lithium metal anode is considerably improved when compared to the standard carbonate-based electrolyte. It decreases the morphology of lithium dendrites and porous lithium metal when combined with the extremely stable F component in SEI, thereby avoiding anode and cathode deterioration. We discovered that the reductive reactions of FEC and FDMA are faster than the decomposition of salt, which can provide a source of F to rapidly consume Li and act as a protective LiF layer from analyzing the trajectory of HAIR MD with clarifying the detailed initial

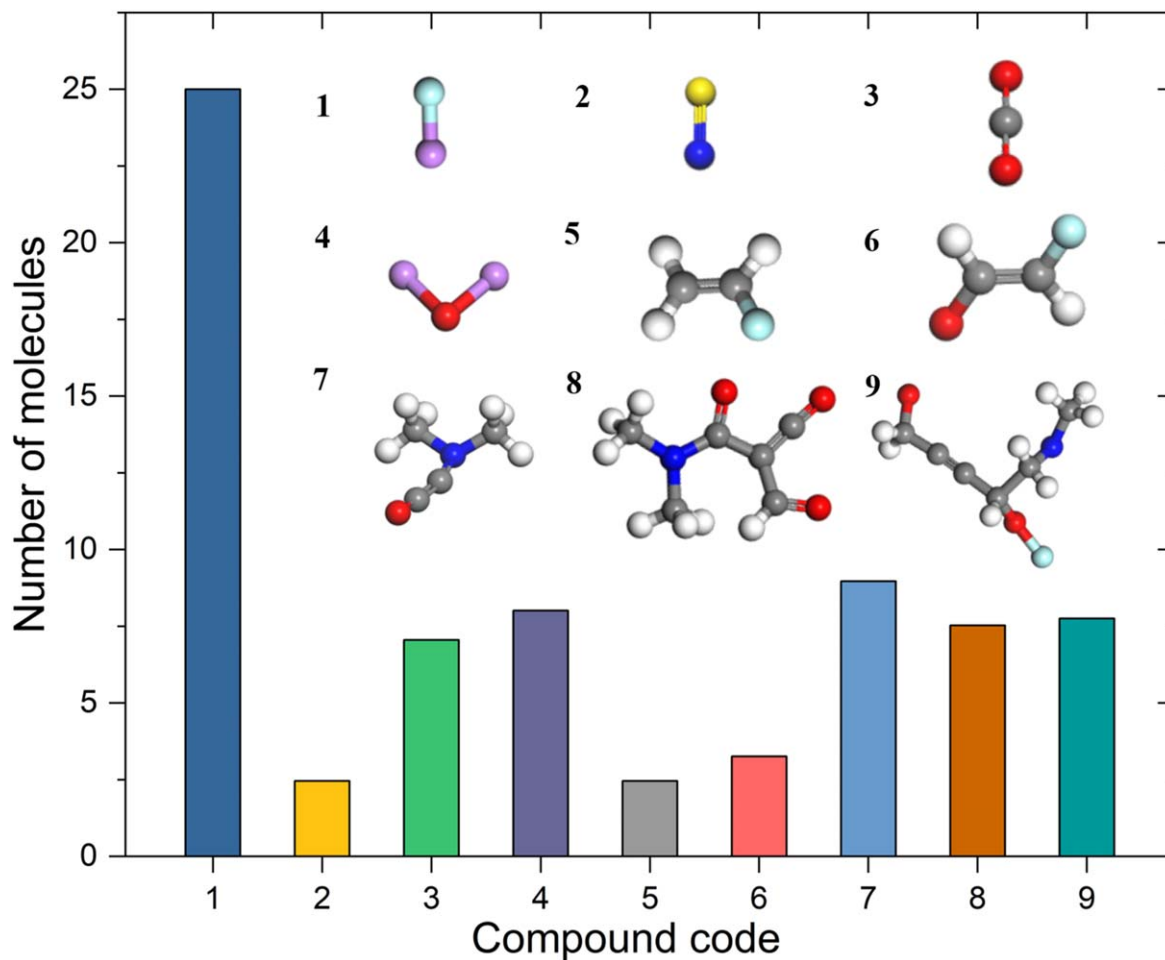


Figure 6. The relative composition of Li-containing species obtained from HAIR simulations within 1 ns. Color code: lithium, purple; oxygen, red; carbon, gray; fluorine, cyan; sulfur, yellow; nitrogen, blue; hydrogen, white.

Table I. Calculated and experimental binding energy values and shift of N1s and F1s.

N1s, F1s	Exp. ²⁴	Simulated 550 ps	Simulated 1 ns	Exp. shift	Simulated 550 ps. shift	Simulated 1 ns. shift
Li _x -N	398.7	375.1	375.0	0.0	0.0	0.0
Li-N-C	402.1	378.2	378.4	3.4	3.1	3.4
N-C ₃	—	378.9	379.0	—	3.8	4.0
Li-F	685.0	655.5	655.2	0.0	0.0	0.0
C-F	687.6	657.9	657.7	2.6	2.4	2.5

reduction mechanism of FDMA, FEC and LiTFSI. The SEI chemistry of the FDMA product is distinct from that of conventional carbonate-based electrolytes since it contains a lot of nitrogen-containing components. Li-N-C and Li_xN in the reduction product. Recent studies have shown that the SEI composition containing organic and inorganic components is more conducive to obtaining better performance lithium batteries, and our results are also in line with this point. Recent research has indicated that an SEI composition including both conductive

organic and inconducive inorganic components is more favorable to higher lithium battery performance, and our findings support this. When reactions continue to occur beyond 550 ps, and the result remains essentially unaltered until 770 ps, the HAIR simulation demonstrates the necessity of increasing the time scale in modeling. The reduction mechanism and detailed structural evolution of SEI provided from HAIR simulation should be of help in providing insights for future electrolyte design.

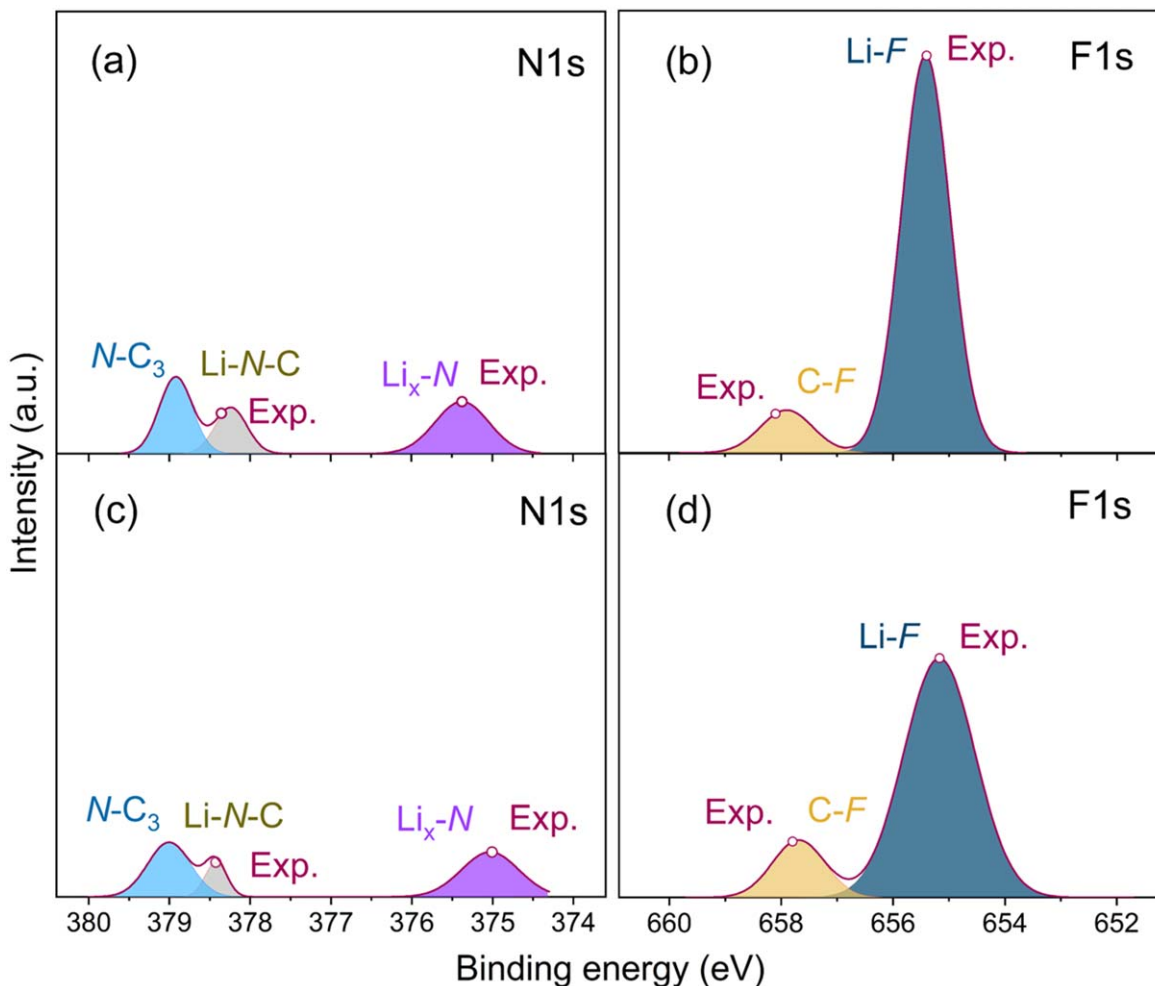


Figure 7. X-ray photoelectron spectroscopy (XPS) of N_{1s} and F_{1s} in different simulated timescale. Figure a and b shows N_{1s} and F_{1s} in this battery system after simulated 550 ps. Figure c and d shows N_{1s} and F_{1s} in this battery system after simulated 1 ns. Wine red dot marked with Exp. represent the experimental binding energy shifts from Ref. 24 and the corresponding values are shown in Table I.

Acknowledgments

T. C. thanks the support from Suzhou Key Laboratory of Functional Nano & Soft Materials, Collaborative Innovation Center of Suzhou Nano Science & Technology, the Priority Academic Program Development of Jiangsu Higher Education Institutions (PAPD), the 111 Project, Joint International Research Laboratory of Carbon-Based Functional Materials and Devices, the National Natural Science Foundation of China (21903058 and 22173066), the Natural Science Foundation of Jiangsu Province (BK20190810).

ORCID

Tao Cheng <https://orcid.org/0000-0003-4830-177X>

References

- J. M. Tarascon and M. Armand, *Nature*, **414**, 359 (2001).
- B. John, Goodenough, and K. S. Park, *J. Am. Chem. Soc.*, **135**, 1167 (2013).
- B. Dunn, H. Kamath, and J. M. Tarascon, *Science*, **334**, 928 (2011).
- H. P. Wu, H. Jia, C. M. Wang, J. G. Zhang, and W. Xu, *Adv. Energy Mater.*, **11**, 2003092 (2021).
- M. Winter, B. Barnett, and K. Xu, "Before li ion batteries." *Chem. Rev.*, **118**, 11433 (2018).
- T. T. Dong et al., *Energy Environ. Sci.*, **11**, 1197 (2018).
- X. B. Cheng, R. Zhang, C. Z. Zhao, and Q. Zhang, *Chem. Rev.*, **117**, 10403 (2017).
- D. C. Lin, Y. Y. Liu, and Y. Cui, *Nat. Nano.*, **12**, 194 (2017).
- W. Xu, J. L. Wang, F. Ding, X. L. Chen, E. Nasybulin, Y. H. Zhang, and J. G. Zhang, *Energy Environ. Sci.*, **7**, 513 (2014).
- C. Huang et al., *Nat. Commun.*, **5**, 3015 (2014).
- F. F. Shi, A. Pei, D. T. Boyle, J. Xie, X. Y. Yu, X. K. Zhang, and Y. Cui, *Proc. Natl. Acad. Sci. U S A*, **115**, 8529 (2018).
- F. Ding et al., *J. Electrochem. Soc.*, **160**, A1894 (2013).
- J. Scheers, S. Fantini, and P. Johansson, *J. Power Sources*, **255**, 204 (2014).
- X. Chen and Q. Zhang, *Acc. Chem. Res.*, **53**, 1992 (2020).
- X. W. Xie, E. W. C. S. Smith, M. J. Wen, H. D. Patel, S. M. Blau, and K. A. Persson, *J. Am. Chem. Soc.*, **143**, 13245 (2021).
- X. Chen, H. R. Li, X. Shen, and Q. Zhang, *Angew. Chem. Int. Ed.*, **57**, 16643 (2018).
- S. Li, M. G. Jiang, Y. Xie, H. Xu, J. L. Jia, and J. Li, *Adv. Mater.*, **30**, 1706375 (2018).
- Y. Z. Li et al., *Science*, **358**, 506 (2017).
- Y. Yamada, J. L. Wang, S. Ko, E. Watanabe, and A. Yamada, *Nat. Energy*, **4**, 269 (2019).
- Y. Yamada, Y. Takazawa, K. Miyazaki, and T. Abe, *J. Phys. Chem. C*, **114**, 11680 (2010).
- K. Yoshida, M. Nakamura, Y. Kazue, N. Tachikawa, S. Tsuzuki, S. Seki, K. Dokko, and M. Watanabe, *J. Am. Chem. Soc.*, **133**, 13121 (2010).
- K. Ueno, K. Yoshida, M. Tsuchiya, N. Tachikawa, K. Dokko, and M. Watanabe, *J. Phys. Chem. B*, **116**, 11323 (2012).
- Y. Yamada, M. Yaegashi, T. Abe, and A. Yamada, *Chem. Commun.*, **49**, 11194 (2013).
- Q. D. Wang et al., *Nat. Commun.*, **11**, 4188 (2020).
- Y. H. Chen, S. A. Freunberger, Z. Q. Peng, F. Barde, and P. G. Bruce, *J. Am. Chem. Soc.*, **134**, 7952 (2012).
- A. P. Wang, S. Kadam, H. Li, S. Q. Shi, and Y. Qi, *NPJ Comput. Mater.*, **4**, 15 (2018).
- E. P. Kamphaus, S. Angarita-Gomez, X. P. Qin, M. H. Shao, M. Engelhard, K. T. Mueller, V. Murugesan, and P. B. Balbuena, *ACS Appl. Mater. Interfaces*, **11**, 31467 (2019).
- L. E. Camacho-Forero, T. W. Smith, and P. B. Balbuena, *J. Phys. Chem. C*, **119**, 26828 (2015).

29. S. Q. Si, J. Gao, Y. Liu, Y. Zhao, Q. Wu, W. W. Ju, C. Y. Ouyang, and R. J. Xiao, *Chinese Phys. B*, **25**, 018212 (2016).
30. E. Crabb, A. France-Lanord, G. Leverick, R. Stephens, Y. Shao-Horn, and J. C. Grossman, *J. Chem. Theory Comput.*, **16**, 7255 (2020).
31. H. Tachikawa, *ChemPhysChem*, **15**, 1604 (2014).
32. Y. Liu, Q. T. Sun, P. P. Yu, Y. Wu, L. Xu, H. Yang, M. Xie, T. Cheng, and W. A. Goddard, *J. Phys. Chem. Lett.*, **12**, 2922 (2021).
33. A. C. T. van Duin, S. Dasgupta, F. Lorant, and W. A. Goddard, *J. Phys. Chem. A*, **105**, 9396 (2001).
34. K. Chenoweth, A. C. T. van Duin, and W. A. Goddard, *J. Phys. Chem. A*, **112**, 1040 (2008).
35. Y. Liu, P. P. Yu, Y. Wu, H. Yang, M. Xie, L. Y. Huai, W. A. Goddard, and T. Cheng, *J. Phys. Chem. Lett.*, **12**, 1300 (2021).
36. Y. Liu, P. P. Yu, Q. T. Sun, Y. Wu, M. Xie, H. Yang, T. Cheng, and W. A. Goddard, *ACS Energy Lett.*, **6**, 2320 (2021).
37. J. P. Perdew, K. Burke, and E. Ernzerhof, *Phys. Rev. Lett.*, **77**, 3865 (1996).
38. S. Naserifar, J. J. Oppenheim, H. Yang, T. T. Zhou, S. Zybin, M. Rizk, and W. A. Goddard, *J. Chem. Phys.*, **151**, 154111 (2019).
39. G. Kresse and D. Joubert, *Phys. Rev. B: Condens. Matter Mater. Phys.*, **59**, 1758 (1999).
40. H. J. Monkhorst and J. D. Pack, *Phys. Rev. B*, **13**, 5188 (1976).
41. S. Plimpton, *J. Comput. Phys.*, **117**, 1 (1995).
42. L. Köhler and G. Kresse, *Phys. Rev. B*, **70**, 16 (2004).
43. J. Qian, A. Baskin, Z. Liu, D. Prendergast, and E. J. Crumlin, *J. Chem. Phys.*, **153**, 044709 (2020).
44. J. Tian, J. Matz, P. Dong, J. F. Shen, and M. X. Ye, *Adv. Energy Mater.*, **11**, 2100046 (2021).